SUPPLEMENTARY INFORMATION for

“Acoustic realization of projective mirror Chern insulators”

Tianzi Li, Luohong Liu, Qicheng Zhang, and Chunyin Qiu*

Key Laboratory of Artificial Micro- and Nano-Structures of Ministry of Education and School of Physics and Technology, Wuhan University, Wuhan 430072, China

* To whom correspondence should be addressed: cyqiu@whu.edu.cn

Supplementary Note 1. Symmetry analysis on our projective mirror Chern insulator

In this section, we introduce first the concept of the projective symmetry, and then provide a symmetry analysis on our projective mirror Chern insulator (PMCI). It is well-known that an ordinary crystalline symmetry can be defined by a spatial operation R keeping the lattice unchanged. In other words, the operation R commutes with the lattice Hamiltonian H_L, $[R, H_L] = 0$. After taking the gauge field into the consideration, however, some ordinary spatial symmetries need to be refined by a gauge transformation G. The lattice Hamiltonian H_L now commutes with the combination of the spatial operation R and the gauge transformation G, $[RG, H_L] = 0$. This new operator $\mathcal{R} = RG$ is the projective symmetry. Specifically, our PMCI model in Fig. 1b preserves ordinary twofold rotation symmetry C_{2z}, projective mirror symmetry $\mathcal{M}_z$, and projective inversion symmetry, whose matrix forms are provided in Supplementary Table 1. In particular, the projective mirror symmetry $\mathcal{M}_z$ has the spinful representation with $\mathcal{M}_z^2 = -1$, which is the essential requirement of constructing PMCIs. Notice that a combination of the projective inversion $\mathcal{P}$ and the time-reversal symmetry $\mathbb{T}$ returns any momentum $\boldsymbol{k}$ to itself (modulo 2π), which satisfies $(\mathcal{P}\mathbb{T})^2 = -1$ and thus enforces the bulk bands doubly degenerate everywhere. Nevertheless, the projective inversion $\mathcal{P}$ is *not* necessary for constructing a PMCI (see Supplementary Fig. 2).

Supplementary Table 1. Symmetries in our PMCI model

C_{2z}	$\sigma_0\tau_1$	${C_{2z}}^{-1}H(\boldsymbol{k})C_{2z} = H(-\boldsymbol{k})$
$\mathcal{M}_z$	$i\sigma_2\tau_0$	${\mathcal{M}_z}^{-1}H(\boldsymbol{k})\mathcal{M}_z = H(\boldsymbol{k})$
$\mathcal{P}$	$i\sigma_2\tau_1$	$\mathcal{P}^{-1}H(\boldsymbol{k})\mathcal{P} = H(-\boldsymbol{k})$
$\mathcal{L}_x$	$\sigma_3\begin{pmatrix} 0 & 1 \\ e^{ik_x} & 0 \end{pmatrix}$	${\mathcal{L}_x}^{-1}H(\boldsymbol{k})\mathcal{L}_x = H(\boldsymbol{k})$

Here, we give some additional comments for the PMCI model introduced in our main text. First, a *minimal* PMCI model requires four bands in total, allowing one pair of gapped bands in each mirror subspace. Therefore, the monolayer model should contain two orbitals in each unit cell. Obviously, when $t_1 = 0$, our monolayer model reduces to the Su-Schrieffer-Heeger model at the phase transition point, which is the simplest two-orbital model. In order to minimize the symmetry of the system (and thus avoid additional degeneracy as much as possible), we consider only a single next-nearest-neighboring coupling t_1 between the monolayer unit cells to open the band gap. This yields the monolayer structure illustrated in

Fig. 1b. Since the interlayer hoppings refrain from being nearest-neighboring ones, we consider only one pair of positive and negative next-nearest-neighboring interlayer hoppings.

Note: For the special case of $t_1 = 0$, our PMCI model has an extra projective translation symmetry $\mathcal{L}_x$ (Supplementary Table 1). At the time-reversal-invariant momenta (TRIMs) X and M, the projective spatial symmetries $\mathcal{L}_x$ and $\mathcal{M}_z$ have representations that commute with $\mathcal{P}T$ symmetry and anticommute with each other, and additionally $\mathcal{L}_x^2 = 1$. The above symmetry algebra will enforce the fourfold degeneracy at the TRIMs X and M (see Ref. 1).

Supplementary Note 2. Mirror Chern number and phase diagram

In this section, we introduce a finite sum method to calculate Chern number and link it to the appearance of 'Dirac fermions' in $\boldsymbol{k}$ space. We first review some important conclusions in Ref. 2 and Ref. 3, and apply them to the PMCI model proposed in our main text.

The references develop a method to determine the Chern number of any two-band model by counting the chirality and the sign of the mass term of the lattice Dirac fermion. We start from a general two-band Hamiltonian $H_2(\boldsymbol{k}) = \boldsymbol{d}(\boldsymbol{k}) \cdot \boldsymbol{\sigma}$. The Chern number of the occupied band can be written as

$$C = \frac{1}{4\pi} \int_{BZ} d^2\boldsymbol{k}\, \widehat{\boldsymbol{d}} \cdot (\partial_{k_x} \widehat{\boldsymbol{d}} \times \partial_{k_y} \widehat{\boldsymbol{d}}), \tag{S1}$$

which is the wrapping number of the map $k \to \widehat{\boldsymbol{d}} = \boldsymbol{d}/|\boldsymbol{d}|$ between the Brillouin zone torus T^2 and the unit sphere S^2. Notably, $\widehat{\boldsymbol{d}}$ can also be thought of as a composition $\widehat{\boldsymbol{d}} = \pi \circ \boldsymbol{h}$ with $\pi: \mathbb{R}^3 \setminus \{(0,0,0)\} \longrightarrow S^2$ and $\boldsymbol{d}: T^2 \longrightarrow \mathbb{R}^3 \setminus \{(0,0,0)\}$. A trick to avoid performing above integration is to relate the Chern number to the Brouwer degree of the map $\widehat{\boldsymbol{d}}$ as

$$C = \sum_{y \in Y_p} \sum_{k \in \widehat{\boldsymbol{d}}^{-1}(y)} \mathrm{sign}[(\partial_{k_x} \boldsymbol{d} \times \partial_{k_y} \boldsymbol{d}) \cdot \boldsymbol{n}], \tag{S2}$$

where p is an arbitrary point on S^2, $\boldsymbol{n}$ is the unit towards p and $Y_p = \mathcal{F} \cap \pi^{-1}(p)$. The general evaluating procedure starts with choosing a point p on S^2 and then determining the intersections of $\mathcal{F}$ with the ray originating from $(0,0,0)$ to p. These intersections typically form a discrete set of Y_p points on $\mathbb{R}^3$. For our purpose, it is very useful to choose p to be on the $\sigma_{\boldsymbol{z}}$ axis. Then the sum in Eq. (S2) must be done over the points that satisfy $d_x(\boldsymbol{k}) = d_y(\boldsymbol{k}) = 0$. The above equation can be further symmetrized by consider the whole axis p instead of the ray p, leading to

$$C = \frac{1}{2} \sum_{\boldsymbol{k_D}} \mathrm{sign}\left[\left(\partial_{k_x} \boldsymbol{d} \times \partial_{k_y} \boldsymbol{d}\right)_z\right] \mathrm{sign}(d_z), \tag{S3}$$

where $\boldsymbol{k_D}$ is the momentum that satisfies $d_x(\boldsymbol{k}) = d_y(\boldsymbol{k}) = 0$. In electronic systems, this equation means that a lattice Dirac fermion located at $\boldsymbol{k_D}$ with mass term d_z and chirality

$\chi(\boldsymbol{k_D}) = \mathrm{sign}\left[\left(\partial_{k_x}\boldsymbol{d} \times \partial_{k_y}\boldsymbol{d}\right)_z\right]$ contributes a topological charge of $1/2$ or $-1/2$ to the Chern number C.

Our four-band PMCI model can be decoupled into two subspaces of opposite mirror eigenvalues $\pm i$, i.e., $H = H_{+i} \oplus H_{-i}$. For each subspace, the Hamiltonian takes the form $H_{\pm i} = \boldsymbol{d}(\boldsymbol{k}) \cdot \boldsymbol{\sigma}$, with $d_x = t_0 + t_0 \cos k_x + t_1 \cos k_y$, $d_y = t_0 \sin k_x + t_1 \sin k_y$, and $d_z = \pm 2 t_c \sin k_y$. The Chern number for the $\pm i$ subspace can be written as

$$C_{\pm i} = \frac{1}{2} \sum_{\boldsymbol{k_D}} \chi(\boldsymbol{k_D}) \mathrm{sign}[d_z(\boldsymbol{k_D})], \tag{S4}$$

where $\chi(\boldsymbol{k_D}) = \mathrm{sign}(t_0 t_c \cos k_x \sin k_y - t_0 t_1 \sin k_x \cos k_y)$ with $\boldsymbol{k_D} = (k_x, k_y)$ determined by $d_x(\boldsymbol{k}) = d_y(\boldsymbol{k}) = 0$. When $t_1 = 0$, all three components of $\boldsymbol{d}(\boldsymbol{k})$ vanishes at the TRIMs X and M, leading to a pair of fourfold degenerate points and ill-defined Eq. (S4). For a nonzero t_1, we notice that d_z is nonzero at general $\boldsymbol{k}$, thus we need to solve the following equations to locate the vortex position,

$$\begin{cases} d_x = t_0 + t_0 \cos k_x + t_1 \cos k_y = 0 \\ d_y = t_0 \sin k_0 + t_1 \sin k_y = 0 \end{cases}. \tag{S5}$$

Although above equations are transcendental equations, they have two analytical real solutions when $0 < \left|\frac{t_1}{t_0}\right| < 2$, i.e.,

$$\begin{cases} k_x = \mathrm{acos}(\frac{t^2-2}{2}) \\ k_y = -\mathrm{acos}(\frac{t}{2}) \end{cases} \text{and} \begin{cases} k_x = -\mathrm{acos}(\frac{t^2-2}{2}) \\ k_y = \mathrm{acos}(\frac{t}{2}) \end{cases}, \tag{S6}$$

where $t = \frac{t_1}{t_0}$ is a dimensionless quantity that characterizes the intralayer couplings, and acos is the inverse trigonometric function arccosine within the range $[0, \pi]$. In other words, there are a pair of Dirac fermions in the first Brillouin zone. When t approaches zero, the Dirac fermions move to $\left(\pi, \frac{\pi}{2}\right)$ and $\left(\pi, -\frac{\pi}{2}\right)$. When t approaches to 2, these Dirac fermions meet with each other at $(0, \pi)$, leading to a topological transition. Due to the annihilation of the Dirac fermions, the Chern number for each subspace now vanishes, yielding a zero mirror Chern number (MCN), which is defined as $C_{\mathrm{M}} = (C_{+i} - C_{-i})/2$. Notably, even in the absence of MCN, the edge states along the *x* direction still exist since the model now has a new topological number, coined as mirror $\mathbb{Z}_2$ number v_m. Note that v_m is essentially a non-orientable topological invariant, which will be discussed in our future work. Combining the Eqs. (S4) and (S6), we can calculate Chern number for each subspace as a finite sum, which further gives rise to the MCN.

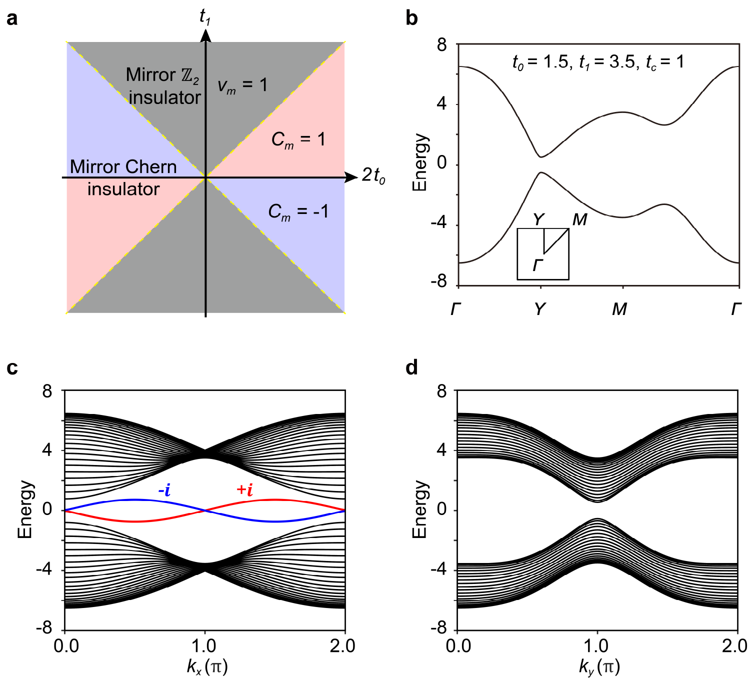

Supplementary Fig. 1 | Phase diagram. a, Phase diagram plotted with the intralayer couplings. The dashed yellow lines indicate the annihilation of the Dirac fermions. **b**, Bulk band structure for a mirror $\mathbb{Z}_2$ insulator with specified parameters. **c-d**, The corresponding ribbon spectra along the x and y directions, respectively. The former features one pair of mirror eigenvalue-locked edge bands for each x-directed boundary, in contrast to the latter without edge states.

Supplementary Fig. 1a shows the phase diagram for our PMCI model, where the phase boundary can be determined analytically by $|t_1| = 2|t_0|$. In addition to the Dirac semimetal phase at the phase boundary, the model supports a nontrivial mirror $\mathbb{Z}_2$ insulator phase and two nontrivial PMCI phases with $C_\mathrm{M} = \pm 1$. Note that the phase diagram is irrelevant to the strength of the interlayer coupling t_c ($t_c > 0$ assumed here); the sign of C_M flips if $t_c < 0$. Moreover, unlike the PMCI phase, the mirror $\mathbb{Z}_2$ insulator features a pair of helical edge states on each x-directed boundary, which are detached from the bulk bands. This can be seen in Supplementary Figs. 1c and 1d.

Supplementary Note 3. Breaking projective inversion symmetry

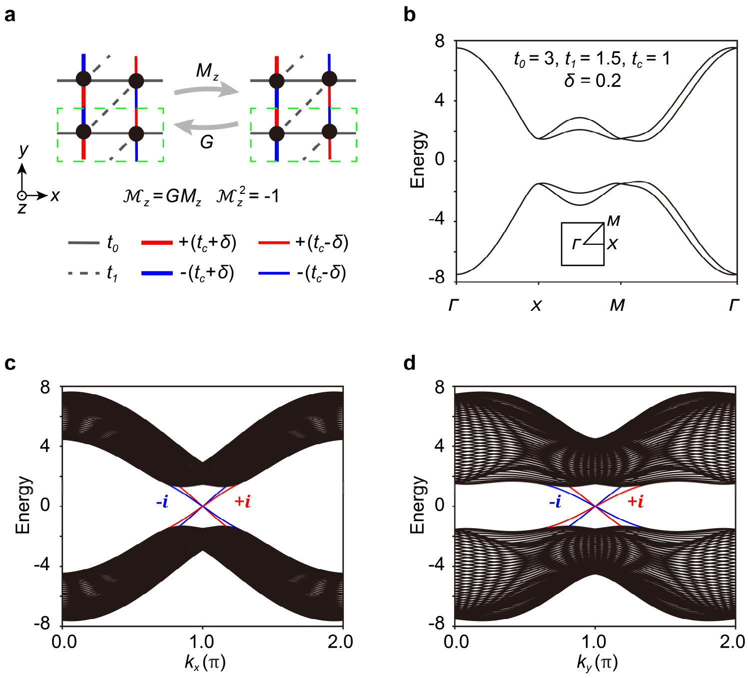

Supplementary Fig. 2 | PMCI without $\mathcal{PT}$ symmetry. a, Tight-binding model extended from that exhibited in Fig. 1b. The amplitudes of the two pairs of interlayer hoppings are modified into $t_c \pm \delta$, which breaks the $\mathcal{PT}$ symmetry yet still preserves the projective mirror symmetry $\mathcal{M}_z$. **b**, Bulk band structure exemplified for $\delta = 0.2$. Now each band is no more twofold degenerate everywhere. **c-d**, The corresponding ribbon spectra along the *x* and *y* directions. Note that the boundary states cannot be mapped with each other by C_{2z} symmetry between the top (left) and bottom (right) boundaries.

The PMCI is robust as long as the system preserves the projective mirror symmetry $\mathcal{M}_z$. Here, as a concrete example, we discuss the effect of $\mathcal{PT}$-breaking perturbation. Supplementary Fig. 2a shows a specific $\mathcal{PT}$-breaking perturbation δ on the tight-binding model in Fig. 1b. The perturbated interlayer hopping reads $T_\delta = T + 2i\delta \sin k_y \tau_0$ and the associated Hamiltonian becomes $H_\delta = H - 2\delta \sin k_y \sigma_2 \tau_0$. Clearly, this perturbated Hamiltonian does not respect $\mathcal{PT}$ symmetry any more. (In this case, the conventional twofold rotation C_{2z} is also broken.) However, the projective mirror symmetry $\mathcal{M}_z$ is still the symmetry of the system, as illustrated in Supplementary Fig. 2a. Supplementary Fig. 2b shows the corresponding bulk spectrum. Due to the absence of $\mathcal{PT}$ symmetry, the bulk bands are no more doubly degenerate at generic $\boldsymbol{k}$. Note that $(\mathcal{M}_z\mathbb{T})^2 = -1$ everywhere, which enforces the double degeneracy of bulk bands at TRIMs. Supplementary Figs. 2c and 2d shows the corresponding x- and y-directed ribbon spectra. Although the boundary states cannot be mapped each other by C_{2z} symmetry between the top (left) and bottom (right) boundaries, the crossing of the edge bands on each boundary is robust under $\mathcal{PT}$-breaking perturbations.

Supplementary Note 4. Design a system with a higher mirror Chern number

Our homobilayer design can be extended to realize the PMCI of a higher MCN. This is demonstrated by the case of $C_m = 2$ below. As sketched in Supplementary Fig. 3a, although the model is also a four-band minimal one, it features more long-range intralayer and interlayer hoppings comparing to the $C_m = 1$ model presented in our main text. Again, the bilayer Hamiltonian formally reads $H = \sigma_0 h + i\sigma_2 T$, where the monolayer Hamiltonian $h = (t_0 + 2t_1 \cos k_y)\tau_1 - 2t_2 \cos(k_x + k_y)\tau_3$ and the interlayer coupling $T = -2it_c \cos k_x \tau_2$. We can perform the similar decomposition process $H = H_{+i} \oplus H_{-i}$, where $H_{\pm i} = \boldsymbol{d}(\boldsymbol{k}) \cdot \boldsymbol{\sigma}$, with $d_x = t_0 + 2t_1 \cos k_y$, $d_y = 2t_c \cos k_x$, and $d_z = \mp 2t_2 \cos(k_x + k_y)$. To analysis the topology in each subspace, we first determine the positions of Dirac fermions $\boldsymbol{k_D} = (k_x, k_y)$ with $d_x(\boldsymbol{k}) = d_y(\boldsymbol{k}) = 0$. Notably, unlike the $C_m = 1$ case, the following equations

$$\begin{cases} d_x = t_0 + 2t_1 \cos k_y = 0 \\ d_y = 2t_c \cos k_x = 0 \end{cases}, \tag{S7}$$

now have four solutions when $0 < \left|\frac{t_0}{t_1}\right| < 2$, i.e.,

$$\begin{cases} k_x = \operatorname{acos}(-\frac{t_0}{2t_1}) \\ k_y = \pm\frac{\pi}{2} \end{cases} \text{and} \begin{cases} k_x = -\operatorname{acos}(-\frac{t_0}{2t_1}) \\ k_y = \pm\frac{\pi}{2} \end{cases}. \tag{S8}$$

The multi-pairs of Dirac fermions with topological charges enable higher Chern number in each subspace, based on Eq. (S4). Combining the Eqs. (S4) and (S8), we can calculate Chern number for each subspace as a finite sum, which further gives rise to the MCN.

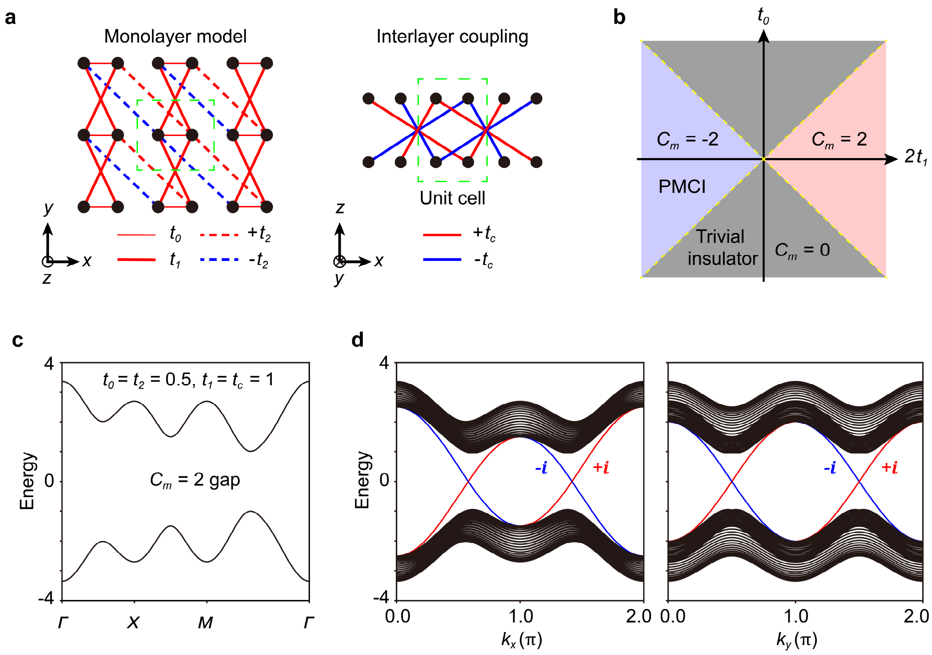

Supplementary Fig. 3 | PMCI designed with a higher MCN ($C_\mathrm{M} = 2$). a, Tight-binding model, where the top view (left) shows the constituent monolayer lattice and the side view sketches the interlayer hoppings. Comparing to the model presented in our main text, more long-range couplings are introduced here. **b**, Phase diagram plotted with the intralayer hoppings t_0 and t_1, where other hoppings are nonzero. **c**, Band structure exemplified for $t_c = t_1 = 1$, $t_0 = 0.5$, and $t_2 = 0.5$. Each band is twofold degenerate. **d**, Edge spectra simulated for ribbon structures with the same parameters in **c**.

Supplementary Fig. 3b shows the corresponding phase diagram. It contains trivial insulator phase and nontrivial PMCI phases (with $C_m = \pm 2$). The phase transition occurs at $|t_0/t_1| = 2$, where the Dirac fermions annihilate pairwise at $\left(\pi, \pm\frac{\pi}{2}\right)$. Note that the phase diagram holds for $t_2 > 0$ and $t_c > 0$; once $t_2 < 0$ or $t_c < 0$, the sign of the MCN will be switched. Supplementary Figs. 3c and 3d demonstrate a concrete example with $C_m = 2$. Different from the $C_m = 1$ case, the system features two pairs of counter-propagated gapless states on each boundary. A PMCI phase with even higher MCN could be constructed by considering more complex lattices and hoppings. Notably, the integer nature of the topological index distinguishes the PMCI band topology from the other time-reversal-invariant topological states, especially from the quantum spin Hall phase.

Supplementary Note 5. Acoustic realization of the projective mirror Chern insulator

In this section, we provide the geometric details of our acoustic PMCI and corresponding fitted tight-binding model. Throughout this work, air density $\rho = 1.29\ \mathrm{kg\ m^{-3}}$ and sound speed $c = 343.5\ \mathrm{m\ s^{-1}}$ are used for full-wave simulations, performed with the commercial software COMSOL Multiphysics (Pressure Acoustics Module).

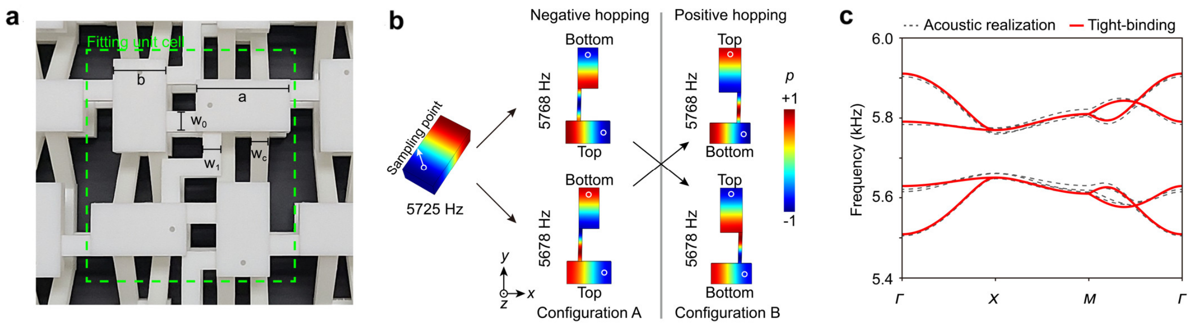

Supplementary Fig. 4 | Acoustic realization of the PMCI. a, Geometry of our acoustic PMCI made of hard-walled air cavities. **b**, Implementation of the positive and negative interlayer couplings, where the top-layer and bottom-layer cavities are positioned perpendicular to each other. Each dipole (cavity) resonator can be characterized by a single sampling point (circle). Opposite hopping signs are achieved by locating the coupling tube at different sides of the horizontal cavities. **c**, B and structure simulated for our acoustic PMCI (grey lines), compared with the fitting result by tight-binding model (red lines).

Supplementary Fig. 4a shows the detailed geometry of our acoustic PMCI, which consists of a rectangular lattice of coupled air cavities. Specifically, each cuboid resonator has a size of $a \times b \times c = 30\ \mathrm{mm}\ \times 15\ \mathrm{mm}\ \times 10\ \mathrm{mm}$, which ensures a dipole resonance of frequency ~5725 Hz far away from the other undesired cavity modes. The connecting tubes have square cross sections and the widths of them are $w_0 = 3.5\ \mathrm{mm}$, $w_1 = 2.5\ \mathrm{mm}$, and $w_c = 2.5\ \mathrm{mm}$, which correspond to the couplings t_0, t_1, and t_c, respectively. The sign of the hoppings, controlled by the spatial positions of the coupling tubes with respect to the cavities, is consistent with those depicted in Fig. 1b (see main text). Supplementary Fig. 4b illustrates the realization of positive and negative *interlayer* couplings, which is crucial to the construction of projective mirror symmetry. It is easy to derive that for two identical resonators coupled with a positive hopping, the resultant eigenmodes will split into an in-phase mode of higher energy and an out-of-phase mode of lower energy. On the contrary, if the resonators are coupled with a negative hopping, the in-phase mode has a lower energy than that of the out-of-phase mode. It can be easily inspected if the two cavities are positioned in parallel (see Ref. 4). A generalized construction is developed in Ref. 5, where the two cavities are coupled perpendicularly to each other. In order to achieve a compact structure for the whole system, here we employ the second approach to construct positive and negative *interlayer* couplings. As shown in Supplementary Fig. 4b, positive and negative hoppings (of exactly the same amplitudes) are achieved by locating the coupling tubes at the left and right sides of the middle line of the horizontal cavity, respectively. In this case, the in-phase and out-of-phase modes can be diagnosed by checking the phases of the two coupled dipoles, where each dipole cavity resonator can be represented by a single sampling point. As shown in Supplementary Fig. 4c, our acoustic system captures well the tight-binding model with onsite energy ≈ 5700 Hz, $t_0 \approx 71$ Hz, $t_1 \approx 60$ Hz, and $t_c \approx 40$ Hz.

Supplementary Note 6. More details in our acoustic experiments

This section provides more experimental details of Figs. 2 and 3 in our main text. The bulk states extraction technique was first developed to extract symmetry information at high symmetry points in Ref. 6. Here, we further use selective-excitation technique to measure the bulk wavefunctions of the degenerate bands over the whole Brillouin zone.

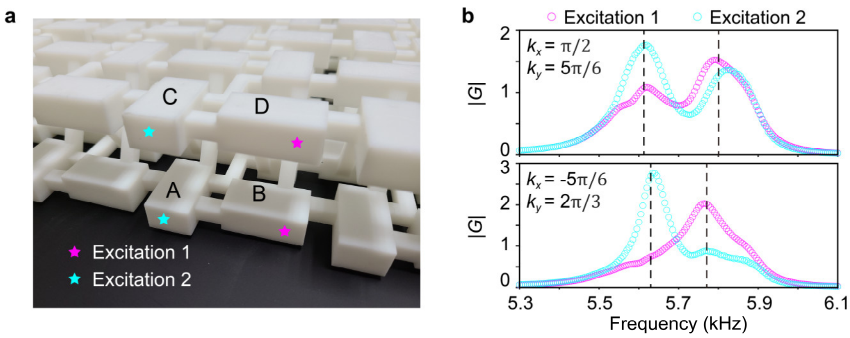

Supplementary Fig. 5 | Experimental details. a, The source configuration used for selective excitation, which is exemplified by the edge measurement for the clarity of demonstration. $\{A, B, C, D\}$ label the four cavities in a unit cell, and the magenta and cyan stars indicate two sets of source positions. **b**, Norm of the Green function $G_\alpha(\boldsymbol{k}, \omega)$ at two specified momenta, measured for the two excitations with $+i$ source. The black dashed lines indicate the predicted eigenfrequencies.

Considering that the eigenstates can be decomposed into two independent subspaces of mirror eigenvalues $m_z = \pm i$, we can selectively excite the eigenstates with specific source configurations. Specifically, the $\pm i$ sources are composed of a pair of broadband point-like sound sources with a phase difference of $\pm\pi/2$ (see main text). The pair of sound sources can be positioned inside the cavities A and B (excitation 1), or C and D (excitation 2), as illustrated by the edge measurement in Supplementary Fig. 5a.

Our experiments were performed for airborne sound at audible frequency. In our bulk measurements, we placed the sound source in the middle of the sample. We used a needle-like microphone (B&K Type 4182) to scan the pressure information inside the cavities one by one, together with another microphone (B&K Type 4138) fixed at the source cavity for phase reference. Both the input and output signals were recorded and frequency-resolved with a multi-analyzer system (B&K Type 3560B). For each type of excitation, we scanned the acoustic response over the sample to extract phase and amplitude information of the acoustic field $\psi_\alpha(n,\omega)$. Here the notations α and n in $\psi_\alpha(n,\omega)$ denotes the cavity α of the n-th unit cell with $\alpha \in \{A, B, C, D\}$, as shown in Supplementary Fig. 5a. To extract the excited bulk states, we evaluated the real-space Green function $g_\alpha(n,\omega) = \langle\psi_\alpha^*(n,\omega)\psi_s\rangle$, where ψ_s denotes the acoustic field detected in one of the two source cavities, and performed Fourier transform to obtain the Green function $G_\alpha(\boldsymbol{k},\omega)$ in momentum space. At each frequency ω, we get a vector $G_{\boldsymbol{k}}(\omega) = (G_A, G_B, G_C, G_D)^\intercal$ in momentum space. In general, the norm of $G_{\boldsymbol{k}}$, which characterizes the sound response to the external source, should reach maximum at the eigenfrequency $\omega_{\boldsymbol{k}}$. This can be seen in the top panel of Supplementary Fig. 5b at the specified momentum. At the predicted eigenfrequencies, $G_{\boldsymbol{k}}$ is proportional to the eigenstates $u_{\boldsymbol{k}}$. However, there are some modes (which carry tiny weights on the sublattices A and B, or C and D) weakly respond to one of the excitation setups, as exemplified in the bottom panel of Supplementary Fig. 5b. To avoid that case, we choose $G_{\boldsymbol{k}}$ of the excitation setup with larger $|G_{\boldsymbol{k}}|$ at $\omega_{\boldsymbol{k}}$, which gives rise to the state vector $u_{\boldsymbol{k}} = G_{\boldsymbol{k}}/|G_{\boldsymbol{k}}|$ in momentum space. Using the selectively-excited wavefunction $u_{\boldsymbol{k}}$, we computed the expectation value of the projective mirror operator, $\bar{\mathcal{M}}_z = \langle u_{\boldsymbol{k}}|\mathcal{M}_z|u_{\boldsymbol{k}}\rangle$, and the Berry curvature distribution of the lower band. An integral over the first Brillouin zone gives the Chern number for each mirror subspace, which contributes the MCN ultimately. Similarly, the wavefunctions and the associated mirror expectation values were measured for the edge states, where the sources were relocated to the middle of the top edge of our sample.

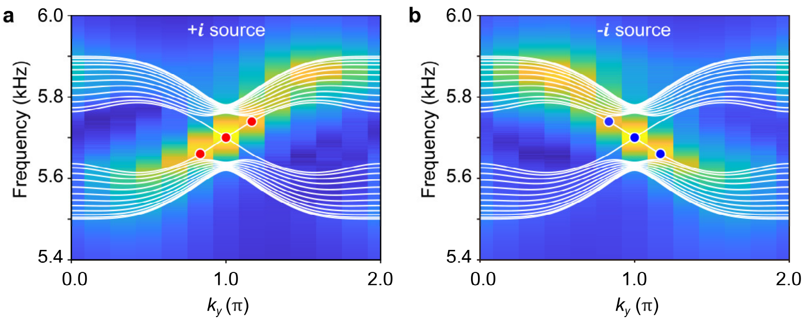

Supplementary Fig. 6 | Edge spectra measured along the *y* direction. a-b, Experimental edge spectra (color scale) selectively excited by the $\pm i$ sources, each of which features one chiral edge band as expected. Theoretical ribbon spectra (white lines) are provided for comparison, along with the measured mirror expectation eigenvalues (color circles).

As a supplement of Fig. 4a, in Supplementary Fig. 6 we present the edge spectra measured for the *right* edge of the sample. Together with Fig. 4c responsible for the top edge, one may expect unidirectional edge states encircling the boundary of a finite-sized sample, as illustrated in Fig. 1c.

References

1. B. J. Wieder and C. L. Kane, Spin-orbit semimetals in the layer groups, Phys. Rev. B **94**, 155108 (2016).
2. D. Sticlet, F. Piéchon, J.-N. Fuchs, P. Kalugin and P. Simon, Geometrical engineering of a two-bands Chern insulator in two dimensions with arbitrary topological index, Phys. Rev. B **85**, 165456 (2012).
3. J. Cayssol and J.-N. Fuchs, Topological and geometrical aspects of band theory, J. Phys. Mater., **4**, 034007 (2021).
4. Y. Qi, et al. Acoustic realization of quadrupole topological insulators, Phys. Rev. Lett. **124**, 206601 (2020).
5. H. Xue, et al. Observation of an acoustic octupole topological insulator, Nat. Commun. **11**, 2442 (2020).
6. V. Peri, et al. Experimental characterization of fragile topology in an acoustic metamaterial, Science **367**, 797 (2020).